Azimuthal anisotropy relative to the participant plane from a multiphase transport model in central $p + \mathrm{Au}$, $d + \mathrm{Au}$, and $^3\mathrm{He} + \mathrm{Au}$ collisions at $\sqrt{s_{NN}} = 200$ GeV

J. D. Orjuela Koop, A. Adare, D. McGlinchey, and J. L. Nagle
Department of Physics, University of Colorado, Boulder, Colorado 80309, USA
(Received 2 February 2015; revised manuscript received 28 July 2015; published 5 November 2015)

Recent data from $p + p$ and $p + \mathrm{Pb}$ collisions at the Large Hadron Collider (LHC), and $d + \mathrm{Au}$ and $^3\mathrm{He} + \mathrm{Au}$ collisions at the Relativistic Heavy Ion Collider (RHIC) reveal patterns that—when observed in the collision of heavy nuclei—are commonly interpreted as indicators of a locally equilibrated system in collective motion. The comparison of these data sets, including the forthcoming results from $p + \mathrm{Au}$ and $p + \mathrm{Al}$ collisions at RHIC, will help to elucidate the geometric dependence of such patterns. It has recently been shown that a multiphase transport model (AMPT) can describe some of these features in LHC data with a parton-parton scattering cross section comparable to that required to describe $A + A$ data. In this paper, we extend these studies by incorporating a full wave-function description of the $^3\mathrm{He}$ nucleus to calculate elliptical and triangular anisotropy moments v_2 and v_3 for $p + \mathrm{Au}$, $d + \mathrm{Au}$, and $^3\mathrm{He} + \mathrm{Au}$ collisions at the RHIC top energy of 200 GeV. We find reasonable agreement with the measured v_2 in $d + \mathrm{Au}$ and $^3\mathrm{He} + \mathrm{Au}$ and v_3 in $^3\mathrm{He} + \mathrm{Au}$ for transverse momentum (p_T) $\lesssim$1 GeV/c, but underestimate these measurements for higher values of p_T. We predict a pattern of coefficients (v_2, v_3) for $p + \mathrm{Au}$, dominated by differences in the number of induced local hot spots (i.e., one, two, or three) arising from intrinsic geometry. Additionally, we examine how this substantial azimuthal anisotropy accrues during each individual evolutionary phase of the collision in the AMPT model. The possibility of a simultaneous description of RHIC- and LHC-energy data, the suite of different geometries, and high multiplicity $p + p$ data is an exciting possibility for understanding the underlying physics in these systems.

DOI: 10.1103/PhysRevC.92.054903 PACS number(s): 25.75.Gz

I. INTRODUCTION

Recent analyses of data from $p + p$ and $p + \mathrm{Pb}$ collisions at the CERN Large Hadron Collider (LHC), as well as from $d + \mathrm{Au}$ and $^3\mathrm{He} + \mathrm{Au}$ at the BNL Relativistic Heavy Ion Collider (RHIC) have revealed the existence of azimuthal particle correlations reminiscent of those observed in $A + A$ collisions [1–6]. In the latter, this signal has been interpreted as evidence for the liquid-like nature of the quark-gluon plasma (QGP)—a locally equilibrated, strongly coupled medium undergoing hydrodynamic expansion with viscosity near the quantum lower bound. However, these results were largely unexpected in $p(d) + A$, long considered control systems to understand initial-state effects in heavier systems.

The success of nearly inviscid hydrodynamics in describing $A + A$ bulk observables makes it natural to ask if droplets of QGP are being formed in small systems, and if the medium created is sufficiently long lived to equilibrate locally and translate initial spatial anisotropies into final-state particle momentum correlations. However, this is not the only possibility, with potentially different physics being able to account for these measurements [7–9]. Further insight into this matter will come from the confrontation of different model calculations with the full data sets available.

It has been found that azimuthal two-particle correlations from high multiplicity $p + p$, $p + \mathrm{Pb}$, $d + \mathrm{Au}$, and $^3\mathrm{He} + \mathrm{Au}$ events exhibit an enhancement around $\Delta\phi \approx 0$ (i.e., near-side), even when the particles have a large separation in pseudorapidity ($\Delta\eta > 2$), where jet contributions are expected to be minimal. There is an additional enhancement from $p + p$ and peripheral $p + \mathrm{Pb}$ ($d + \mathrm{Au}$) to central $p + \mathrm{Pb}$ ($d + \mathrm{Au}$) around $\Delta\phi \approx \pi$ (i.e., away side) that has been interpreted as the full azimuthal continuation of elliptical- and triangular-flow coefficients, v_2 and v_3. Alternative readings of the away-side pattern include modification of the dijet correlations for the most central $d + \mathrm{Au}$ collisions [10].

Predictions for LHC-energy $p + \mathrm{Pb}$ anisotropies using nearly inviscid hydrodynamics [11] provide a reasonable description of the flow coefficients measured at the LHC. However, as expected, an exact quantitative description depends on on the ratio of shear viscosity to entropy density (η/s) and the details of how initial geometry is modeled, for which there are quite different possibilities in $p + A$ collisions—see, for example, Refs. [12,13]. There are also competing calculations where final-state QGP or flow effects are deemed negligible, and it is initial-state glasma diagrams that give rise to the correlations [9]. In $d + \mathrm{Au}$ and $^3\mathrm{He} + \mathrm{Au}$ collisions, the initial geometry is dominated by the spatial separation of the two nucleons in the deuteron, reducing differences between models of geometry. For this case, nearly inviscid hydrodynamic calculations give a reasonable description of the experimentally extracted flow coefficients [13–15].

However, questions regarding the validity of the near-inviscid hydrodynamic calculations have been raised in terms of the expansion around steep energy density gradients in these small systems [16–19]. It is thus quite interesting that incoherent elastic parton-parton scattering—as implemented in a multiphase transport model (AMPT) [20]—can effectively reproduce the long-range azimuthal correlations [8] and v_2 coefficients [7] observed in high-multiplicity $p + p$ and $p + \mathrm{Pb}$ events at the LHC. Notice, however, that in the case of v_2 in $p + \mathrm{Pb}$, a good reproduction of the measured values is only achieved for $p_T \lesssim 2\,\mathrm{GeV}/c$, above which the calculations underestimate the data. These AMPT results were obtained by using a parton-scattering cross section of $\sigma = 1.5$ to 3.0 mb,

and incorporating the so-called *string melting* mechanism in the model (thus including a time stage dominated by parton-parton scattering).

These results raise the question of whether a similar description can be achieved for different collision geometries at the RHIC energy scale. In particular, we use AMPT to simulate $p+\mathrm{Au}$, $d+\mathrm{Au}$, and $^3\mathrm{He}+\mathrm{Au}$ at $\sqrt{s_{NN}}=200$ GeV since they have been proposed as an excellent testing ground to disentangle the properties of the medium created in small collision systems [14]. In this paper, we begin by describing the AMPT model and the methodology used to compute azimuthal anisotropies of final-state hadrons with respect to the participant plane. We then compare our v_2 and v_3 results in $d+\mathrm{Au}$ and $^3\mathrm{He}+\mathrm{Au}$ to available data, and present predictions for v_2 and v_3 in $p+\mathrm{Au}$. Finally, we discuss our results and provide some conclusions.

II. METHODS

The AMPT event generator [20] is a useful tool for the study of heavy-ion collision dynamics. The AMPT model uses the HIJING model [21] just to generate initial conditions via Monte Carlo Glauber, Zhang's parton cascade (ZPC) to model partonic scattering, and a relativistic-transport (ART) to model late-stage hadronic scattering. We use the AMPT model with string melting turned on, such that a stage with parton-parton scattering is included and subsequent hadronization is described via a coalescence model. In this coalescence model, quark-antiquark pairs and sets of three (anti) quarks in close spatial proximity are grouped to form mesons and baryons, respectively.

In order to better understand how AMPT translates anisotropies in the initial geometry to anisotropies in final-state momentum, we modified the internal Monte Carlo Glauber to more closely resemble the standard approach described in Refs. [22,23], and used in Ref. [14]. The position of nucleons in each colliding nucleus is sampled from the appropriate wave function on an event-by-event basis, after which a nucleon-nucleon inelastic cross section of 42 mb is used to geometrically determine which nucleons were wounded in the collision. In the case of the deuteron, coordinates are sampled from the two-nucleon Hulthén wave function; in the case of ^{3}He, coordinates are obtained with Green's function Monte Carlo calculations using the AV18 + UIX model of three-body interactions [24].

We have run approximately 10 million central (i.e., impact parameter $b<2$ fm) AMPT events with a parton-parton scattering cross section $\sigma=1.5$ mb for each system at $\sqrt{s_{NN}}=200$ GeV. There are numerous publications utilizing the AMPT model to describe $A+A$ collisions at RHIC, quoting a full range of input-cross-section values ranging from $\sigma=1.5$ mb up to $\sigma=10$ mb [25–27]. For this study, we have chosen the smallest value from this range to understand how a minimum parton scattering stage contributes to collective motion in these small systems. Table I summarizes the mean number of nucleon participants for each system in AMPT, as well as the corresponding yield of partons at the end of the parton-scattering stage and the yield of final-state hadrons at the end of the hadronic scattering stage. Note that all partons reported by AMPT at the end of the parton-scattering stage are quarks and antiquarks, and no gluons, which are then input to the particular coalescence calculation for hadronization.

TABLE I. Particle production and eccentricity in central AMPT small-system collisions. For each collision system, we show the mean number of participant nucleons per event, the mean number of partons (i.e., quarks and antiquarks) at freeze-out, the mean number of hadrons after the hadron cascade, and the mean elliptical and triangular initial-state eccentricities.

System	$\langle N_{\mathrm{part}}\rangle$	$\langle N_{\mathrm{partons}}\rangle$	$\langle N_{\mathrm{hadrons}}\rangle$	$\langle\varepsilon_2\rangle$	$\langle\varepsilon_3\rangle$
$p+\mathrm{Au}$	10.45	182	131	0.24	0.16
$d+\mathrm{Au}$	18.3	336	233	0.57	0.17
$^3\mathrm{He}+\mathrm{Au}$	22.3	446	326	0.48	0.23

For each collision system, we compute the eccentricity ε_n, and participant plane angle Ψ_n on an event-by-event basis by using the initial-state coordinates (r_i,ϕ_i) of participant nucleons with the spatial distribution of a Gaussian of width $\sigma=0.4$ fm, as follows for $n=2,3$:

$$\varepsilon_n=\frac{\sqrt{\langle r^2\cos(n\phi)\rangle^2+\langle r^2\sin(n\phi)\rangle^2}}{\langle r^2\rangle}, \tag{1}$$

$$\Psi_n=\frac{\mathrm{atan}[2(\langle r^2\sin(n\phi)\rangle,\langle r^2\cos(n\phi)\rangle)]}{n}+\frac{\pi}{n}. \tag{2}$$

Average values of ε_2 and ε_3 for central $p+\mathrm{Au}$, $d+\mathrm{Au}$, and $^3\mathrm{He}+\mathrm{Au}$ are shown in Table I.

Having measured Ψ_n from the initial-state geometry, we compute the second- and third-order azimuthal anisotropy moments v_2 and v_3 of final-state unidentified charged hadrons within $|\eta|<2$, with respect to the participant planes, as follows:

$$v_n=\langle\cos[n(\varphi-\Psi_n)]\rangle. \tag{3}$$

In addition to extracting anisotropy moments with respect to the participant plane, we are also interested in qualitatively examining the long-range azimuthal correlations of these hadrons. To that end, we follow an analysis procedure similar to that put forth by the ATLAS experiment for $p+\mathrm{Pb}$ collisions in Ref. [3]. We take all final-state charged particles and consider all pairs separated by $2.0<|\Delta\eta|<3.0$ within a common p_T bin. We then form a long-range two-particle azimuthal correlation function for each p_T bin:

$$C(\Delta\phi,p_T)=\frac{1}{N_{\mathrm{trig}}}\frac{dN(p_T)}{d\Delta\phi}. \tag{4}$$

Shown in the top panel of Fig. 1 are the two-particle correlations from $p+p$ and central $^3\mathrm{He}+\mathrm{Au}$ collisions for particles within $0.9<p_T<1.04$ GeV/c. As expected, a flat near-side (around $|\Delta\phi|\approx 0$) distribution is observed in $p+p$ since two particles from the same jet fragmentation or resonance decay are very unlikely to be separated by more than two units of pseudorapidity. There is also a significant $p+p$ away-side enhancement (around $|\Delta\phi|\approx\pi$) from jets back to back at leading order in azimuth and with a significant pseudorapidity swing between them from an imbalance in the initial parton momentum fractions x_1 and x_2.

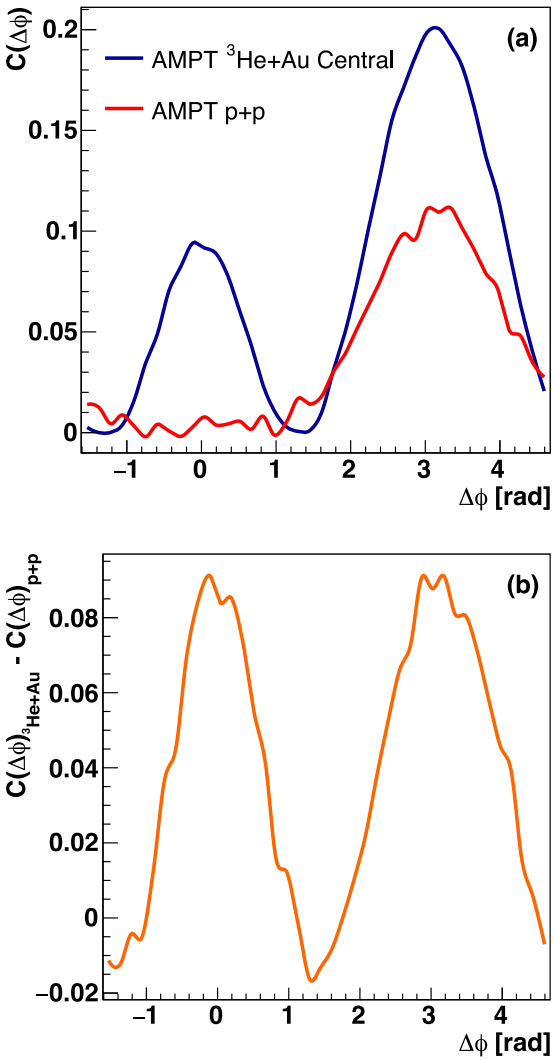

FIG. 1. (Color online) (a) Two-particle correlation for charged particles within $0.90 < p_T < 1.04$ GeV/c for $p+p$ and ^{3}He + Au events at $\sqrt{s_{NN}} = 200$ GeV. (b) Contributions to the correlation function arising from jet fragmentation are removed by subtracting away the per-trigger yield from $p+p$ events. The resulting correlation function is shown in yellow.

In contrast, in the ^{3}He + Au distribution we observe a prominent near-side peak and a nearly-two-fold enhancement of the away-side yield relative to $p+p$. Assuming the jet contribution to be the same in $p+p$ and ^{3}He + Au, we subtract the two distributions, thus obtaining the result shown in the bottom panel of Fig. 1. We choose to use $p+p$ data for the jet subtraction, analogously to what has been done in experimental data with peripheral $p+$Pb ($d+$Au) events [3,4,28]. It is important to note that we do not use long-range two-particle correlations to extract anisotropy moments, but rather to provide a qualitative comparison with experimental results where similar correlations are presented. Hence, all results presented in the remainder of this article are computed with respect to the participant plane by using initial-state geometry, as previously described.

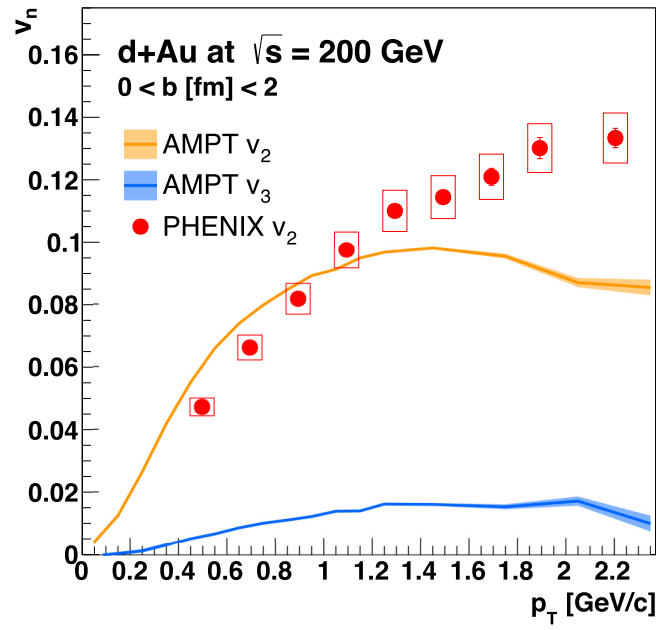

FIG. 2. (Color online) AMPT calculation results for the azimuthal anisotropy moments v_2 and v_3 for central $d+$Au at $\sqrt{s_{NN}} =$ 200 GeV, compared with experimental results from the PHENIX experiment.

III. RESULTS

The resulting anisotropy moments v_2 and v_3 for AMPT $d+$Au central collisions, computed with respect to the participant plane as described in Sec. II, as a function of p_T are shown in Fig. 2. We observe a substantial v_2 that rises with p_T to around 10% at $p_T \approx 1.0$ GeV/c, after which it levels off and even exhibits a slight decrease. The v_3 coefficients exhibit a similar p_T dependent trend, although substantially smaller values. Shown for comparison are elliptic-flow measurements using the participant plane method for central (0%–5%) $d+$Au events at $\sqrt{s_{NN}} = 200$ GeV from the PHENIX experiment [1]. There is a reasonable agreement between the AMPT calculation and the v_2 data below $p_T \approx 1.0$ GeV/c, above which our calculation underestimates the experimental measurements.

Leaving all AMPT parameters fixed, we show in Figs. 3 and 4 the v_2 and v_3 anisotropy moments as a function of p_T for central $p+$Au and ^{3}He + Au, respectively. The same general pattern of rising v_2 with p_T and smaller v_3 coefficients are observed for all systems. It is notable that there is an inflection point at $p_T \approx 1.5$ GeV/c, after which both v_2 and v_3 exhibit a slight decreasing trend.

In 2014, the RHIC experiments completed taking ^{3}He + Au collision data at $\sqrt{s_{NN}} = 200$ GeV. The PHENIX collaboration has presented v_2 and v_3 measurements in ^{3}He + Au at $\sqrt{s_{NN}} =$ 200 GeV [2]. These experimental results are reproduced in Fig. 4 and are found to be in reasonable agreement with the AMPT-extracted coefficients up to $p_T \approx 1.0$ GeV/c, beyond which the AMPT results fall significantly below the data, substantially more for v_3 than for v_2 if we consider the relative difference.

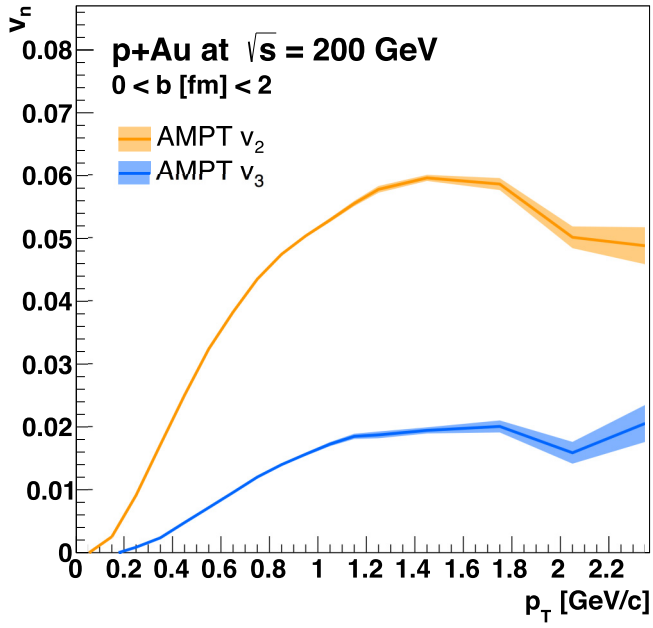

FIG. 3. (Color online) AMPT calculation results for the azimuthal anisotropy moments v_2 and v_3 for central $p + \mathrm{Au}$ at $\sqrt{s_{NN}} = 200$ GeV.

IV. DISCUSSION

Having obtained v_2 and v_3 for collision systems with different initial geometry and having compared them with experimental data, the question is then how to understand these results physically. In hydrodynamic models there is a straightforward physical picture of momentum anisotropy in terms of the velocity field of an expanding fluid. However, the situation is less clear in the case of transport models, such as AMPT. It has recently been proposed that the origin of the substantial v_2 calculated with AMPT lies predominantly in the anisotropic probability of partons to escape from the partonic-scattering phase; that is, there is a preferential direction along which to freeze-out [29]. In this section, we compare our elliptical and triangular anisotropy moments to understand how they relate to intrinsic initial geometry in AMPT.

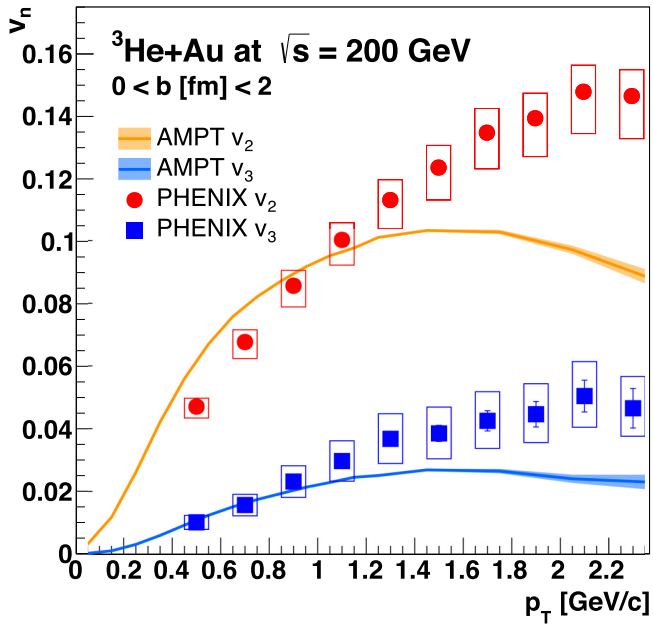

FIG. 4. (Color online) AMPT calculation results for the azimuthal anisotropy moments v_2 and v_3 for central $^3\mathrm{He} + \mathrm{Au}$ at $\sqrt{s_{NN}} = 200$ GeV, compared with experimental results from the PHENIX experiment.

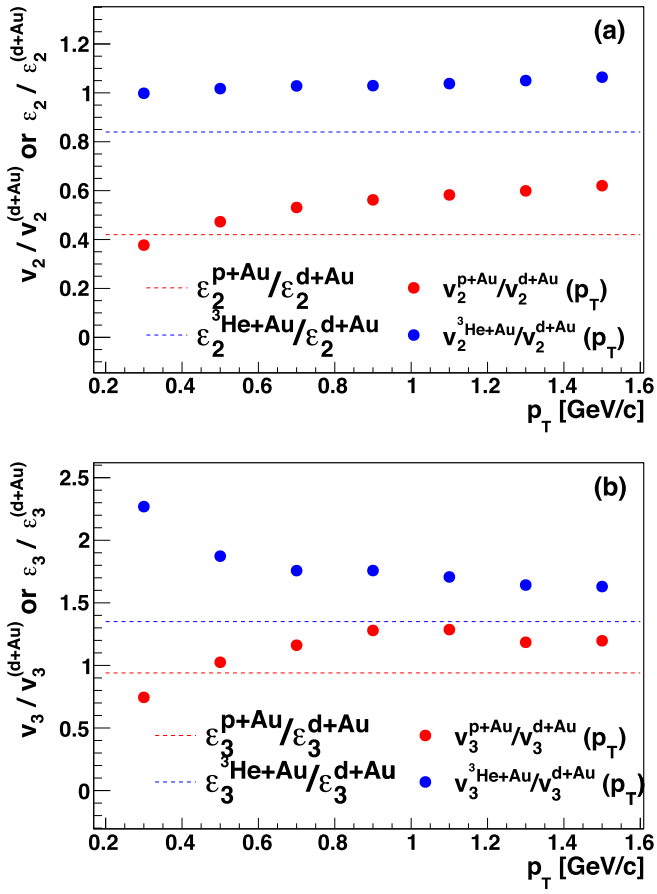

FIG. 5. (Color online) (a) Ratio of elliptic and (b) triangular anisotropy moments as a function of p_T in $p + \mathrm{Au}$ and $^3\mathrm{He} + \mathrm{Au}$ compared with a baseline in $d + \mathrm{Au}$. Dashed lines are the ratios of ε values from the initial geometry.

In hydrodynamic modeling, the final momentum anisotropies are directly related to the initial-state eccentricities. In order to explore whether this relationship holds in AMPT, we take the ratios of AMPT calculated v_2 and v_3 values between systems. Figure 5 (top panel) shows the ratio of v_2 values as a function of p_T in $p + \mathrm{Au}$ and $^3\mathrm{He} + \mathrm{Au}$ relative to $d + \mathrm{Au}$. Figure 5 (bottom panel) shows the ratio of v_3 values as a function of p_T in $p + \mathrm{Au}$ and $^3\mathrm{He} + \mathrm{Au}$ relative to $d + \mathrm{Au}$. Also shown are the ratios of initial eccentricities, ε_2 and ε_3 from Table I, as dashed lines. The AMPT v_2 and v_3 ratios between different systems are relatively independent of p_T, with notable deviations at lower $p_T < 0.6$ GeV/c, and following the same ordering as the initial geometry ratios.

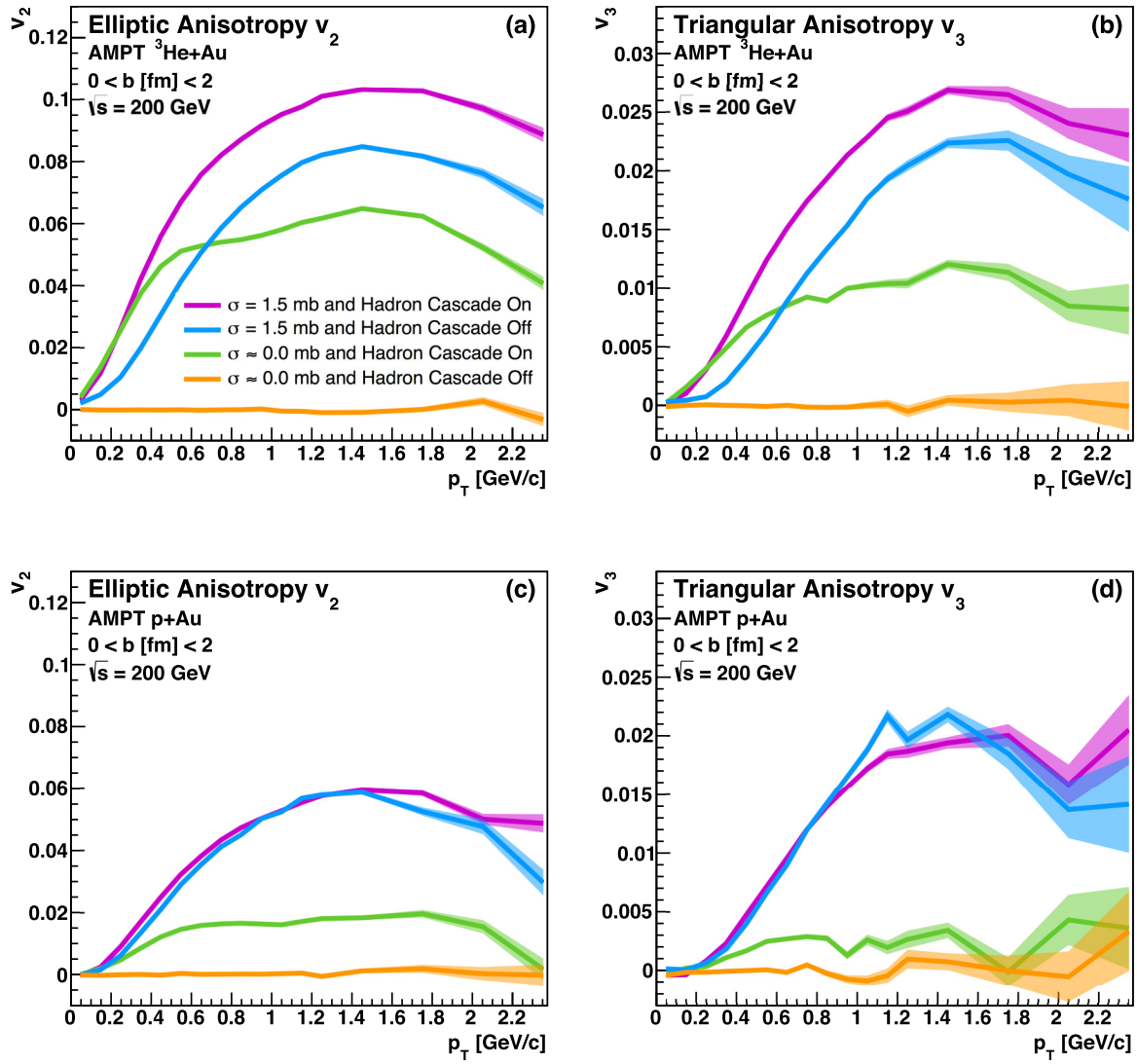

FIG. 6. (Color online) Effects on v_n of enabling and disabling the parton-scattering phase and the hadronic cascade in AMPT for (a), (b) ^{3}He + Au, and (c), (d) p + Au.

The values for the ε ratios are all lower than the AMPT v_n ratios by approximately 15% to 35%. It is notable that the initial spatial eccentricities are calculated from the nucleons, and there will be minor variations in the geometry upon string melting in AMPT. However, reasonable variations in the smearing parameter $\sigma = 0.4$ fm cannot resolve the full differences.

The v_2 in p + Au is predicted to be substantially smaller than in d + Au and ^{3}He + Au and the v_3 in ^{3}He + Au is predicted to be substantially larger than in p + Au and d + Au, both from simple geometry. Although we have qualitatively confirmed the expected scaling of momentum anisotropy with initial geometry across a variety of small collision systems, the exact mechanism responsible for the anisotropies and the deviations from geometry scaling, for example at low p_T, must lie within the inner workings of the AMPT model.

Several authors have identified partonic scattering as the critical mechanism for the development of v_n in this context [7,8,29]. However, partonic scattering is only the first stage in the evolution of the partons that emerge from string melting, and it is relevant to examine the effects that hadronization via coalescence and the subsequent hadron cascade have on the final v_n values.

To that end, we repeat our calculations for ^{3}He + Au and p + Au, enabling and disabling the hadronic cascade, and effectively turning off partonic scattering by setting the parton cross section to very nearly zero. The results are shown in Fig. 6. The first noteworthy feature in the top panels, corresponding to ^{3}He + Au, is that keeping the partonic scattering phase with $\sigma = 1.5$ mb, but turning off the hadron cascade has a substantial effect on v_n. In fact, the blue and violet curves show that a late-stage hadron cascade actually increases v_2 by about 20% for $p_T > 1$ GeV/c and by roughly 100% for $p_T < 0.5$ GeV/c. This effect is even more pronounced for v_3. Additionally, the green curves show that, even when the partonic phase is turned off, a sizable v_2 and v_3 still develop by virtue of final-state hadronic interactions, with the effect being more pronounced for v_3. Finally, as a consistency check,

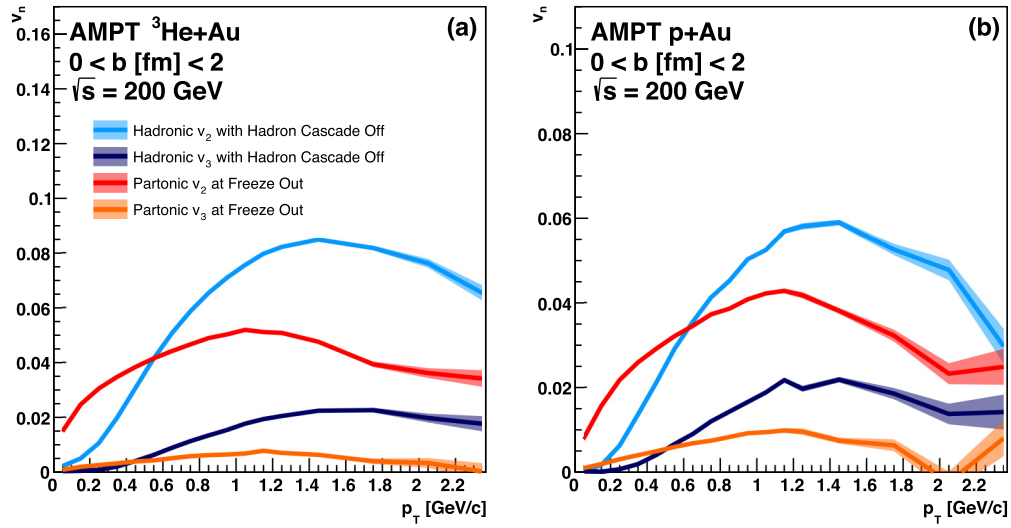

FIG. 7. (Color online) Elliptic and triangular anisotropy moments in (a) ^{3}He + Au and (b) p + Au collisions following partonic scattering using partons immediately prior to hadronization and hadrons immediately after hadronization via coalescence.

disabling both the parton and the hadron cascades results in the collapse of v_n, as shown by the orange curves.

The same analysis is carried out for p + Au in the bottom panels of Fig. 6. We observe that including a hadron cascade after the partonic scattering phase has a much smaller effect on the measured v_2 or v_3. Furthermore, the v_n that develops from the hadron cascade alone when turning off partonic scattering is much less substantial than in the case of ^{3}He + Au, as evidenced by the green curves, showing that in p + Au the bulk of the v_n originates in the parton cascade.

We now examine the role of hadronization in the development of v_n. Figure 7 shows v_2 and v_3 calculated for ^{3}He + Au and p + Au collisions with a partonic scattering phase using (i) partons at freeze-out and (ii) hadrons immediately after coalescence. For high p_T, we observe that hadronization increases v_2 and v_3 in both collision systems. However, for $p_T < 0.5$ GeV/c, the effect of hadronization is to reduce v_n, as evidenced by the crossing of the curves in the figure. This can be understood in terms of quark-coalescence dynamics. Since hadrons are produced by aggregating partons in spatial proximity and with collimated momenta, the coalescence yields hadrons with transverse momentum greater than that of their constituent quarks, hence increasing v_n at higher p_T. It is notable that this effect is greater in p + Au than in ^{3}He + Au.

The detailed mechanism and its relation to the number of parton scatterings in the early AMPT stage still require further elucidation. That said, it is clear that the AMPT coalescence prescription and following hadronic cascade substantially modify and amplify this early stage effect. Therefore, the deviations from geometric scaling shown in Fig. 5 appear to arise from the relative dominance of these stages as a function of p_T and collision system.

V. SUMMARY

Recent intriguing experimental observations at RHIC and the LHC have raised the question of whether small droplets of QGP can be formed in small collision systems. From among several competing models, nearly inviscid hydrodynamic calculations, both at RHIC and the LHC, give reasonable account of the measured anisotropy coefficients. However, parton scattering in transport models—AMPT with string melting, in particular—has also been shown to provide an adequate description of the long-range azimuthal correlations and momentum anisotropy coefficients measured in $p + p$ and p + Pb at LHC energies. In this paper, we extend these calculations to RHIC energies, focusing on the insight that can be gained by varying the initial geometry of the projectile nucleus.

We find that AMPT is capable of reasonably reproducing the measured elliptic and triangular-flow coefficients for central d + Au and ^{3}He + Au collisions at $\sqrt{s_{NN}} = 200$ GeV for $p_T < 1$ GeV/c. However, AMPT underestimates the measured values for higher p_T. With this observation, we ascertain the validity of the model for rendering initial geometric anisotropy into final-state particle momentum correlations for small systems at both the RHIC and LHC energy scales. We also make predictions for elliptic and triangular anisotropy coefficients in p + Au collisions at $\sqrt{s_{NN}} = 200$ GeV and qualitatively relate these results to calculated initial-state geometric anisotropy.

However, we also find that partonic scattering is not the only source of the substantial elliptic and triangular momentum anisotropies in the AMPT model. Hadronization and the subsequent hadron cascade exert important modifications on the v_n from partonic scattering, with strong dependencies both on p_T and the intrinsic initial geometry of the system. Direct comparisons with experimental data in these new systems, with both AMPT and various hydrodynamic models, is anticipated to shed light on the physical dynamics involved in these collision systems. To finalize, we highlight the need to identify additional observables that provide a more stringent discrimination between initial geometry and its translation to final-state correlations.

ACKNOWLEDGMENTS

We acknowledge funding from the Division of Nuclear Physics of the US Department of Energy under Grant No. DE-FG02-00ER41152. We also thank Paul Romatschke, Paul Stankus, Shengli Huang, and Zi-Wei Lin for useful discussions.

[1] PHENIX Collaboration, A. Adare *et al.*, Measurement of Long-range Angular Correlation and Quadrupole Anisotropy of Pions and (Anti) Protons in Central $d+$Au Collisions at $\sqrt{s_{\rm NN}} =$ 200 GeV, Phys. Rev. Lett. **114**, 192301 (2015).

[2] PHENIX Collaboration, A. Adare *et al.*, Measurements of Elliptic and Triangular Flow in High-Multiplicity ^{3}He + Au Collisions at $\sqrt{s_{NN}} = 200$ GeV, Phys. Rev. Lett. **115**, 142301 (2015).

[3] ATLAS Collaboration, G. Aad *et al.*, Observation of Associated Near-Side and Away-Side Long-Range Correlations in $\sqrt{s_{NN}} =$ 5.02 TeV Proton-Lead Collisions with the Atlas Detector, Phys. Rev. Lett. **110**, 182302 (2013).

[4] ALICE Collaboration, B. Abelev *et al.*, Long-range angular correlations on the near and away side in pPb collisions at $\sqrt{s_{NN}} = 5.02$ TeV, Phys. Lett. B **719**, 29 (2013).

[5] CMS Collaboration, S. Chatrchyan *et al.*, Observation of long-range, near-side angular correlations in pPb collisions at the {LHC}, Phys. Lett. B **718**, 795 (2013).

[6] CMS Collaboration, V. Khachatryan *et al.*, Observation of long-range, near-side angular correlations in proton-proton collisions at the LHC, J. High Energy Phys. 09 (2010) 091.

[7] A. Bzdak and G.-L. Ma, Elliptic and Triangular Flow in p-Pb and Peripheral Pb-Pb Collisions from Parton Scatterings, Phys. Rev. Lett. **113**, 252301 (2014).

[8] G.-L. Ma and A. Bzdak, Long-range azimuthal correlations in proton-proton and proton-nucleus collisions from the incoherent scattering of partons, Phys. Lett. B **739**, 209 (2014).

[9] K. Dusling and R. Venugopalan, Azimuthal Collimation of Long-Range Rapidity Correlations by Strong Color Fields in High-Multiplicity Hadron-Hadron Collisions, Phys. Rev. Lett. **108**, 262001 (2012).

[10] L. Adamczyk *et al.*, Effect of event selection on jet-like correlation measurement in $d+$Au collisions at $\sqrt{s_{\rm NN}} = 200$ GeV, Phys. Lett. B **743**, 333 (2015).

[11] P. Bożek, Collective flow in p-Pb and d-Pb collisions at TeV energies, Phys. Rev. C **85**, 014911 (2012).

[12] S. Schlichting and B. Schenke, The shape of the proton at high energies, Phys. Lett. B **739**, 313 (2014).

[13] A. Bzdak, B. Schenke, P. Tribedy, and R. Venugopalan, Initial-state geometry and the role of hydrodynamics in proton-proton, proton-nucleus, and deuteron-nucleus collisions, Phys. Rev. C **87**, 064906 (2013).

[14] J. L. Nagle, A. Adare, S. Beckman, T. Koblesky, J. O. Koop, D. McGlinchey, P. Romatschke, J. Carlson, J. E. Lynn, and M. McCumber, Exploiting Intrinsic Triangular Geometry in Relativistic ^{3}He + Au Collisions to Disentangle Medium Properties, Phys. Rev. Lett. **113**, 112301 (2014).

[15] P. Bozek and W. Broniowski, Hydrodynamic models of ultrarelativistic collisions, Acta Phys. Pol., B **45**, 1337 (2014).

[16] P. Romatschke, Collective flow without hydrodynamics: simulation results for relativistic ion collisions, Eur. Phys. J. C **75**, 429 (2015).

[17] P. Romatschke, Light-heavy ion collisions: A window into pre-equilibrium QCD dynamics?, Eur. Phys. J. C **75**, 305 (2015).

[18] H. Niemi and G. S. Denicol, How large is the Knudsen number reached in fluid dynamical simulations of ultrarelativistic heavy ion collisions? arXiv:1404.7327 [nucl-th] (2014).

[19] G. S. Denicol, C. Gale, and S. Jeon, The domain of validity of fluid dynamics and the onset of cavitation in ultrarelativistic heavy ion collisions, PoS **(CPOD2014)**, 033 (2014).

[20] Z.-W. Lin, C. M. Ko, B.-A. Li, B. Zhang, and S. Pal, Multiphase transport model for relativistic heavy ion collisions, Phys. Rev. C **72**, 064901 (2005).

[21] X.-N. Wang and M. Gyulassy, HIJING 1.0: A Monte Carlo program for parton and particle production in high-energy hadronic and nuclear collisions, Comput. Phys. Commun. **83**, 307 (1994).

[22] M. L. Miller, K. Reygers, S. J. Sanders, and P. Steinberg, Glauber modeling in high-energy nuclear collisions, Annu. Rev. Nucl. Part. Sci. **57**, 205 (2007).

[23] C. Loizides, J. Nagle, and P. Steinberg, Improved version of the PHOBOS Glauber Monte Carlo, SoftwareX **1-2**, 13 (2015).

[24] J. Carlson and R. Schiavilla, Structure and dynamics of few-nucleon systems, Rev. Mod. Phys. **70**, 743 (1998).

[25] STAR Collaboration, L. Adamczyk *et al.*, Inclusive charged hadron elliptic flow in Au + Au collisions at $\sqrt{s_{NN}} =$ 7.7,39 GeV, Phys. Rev. C **86**, 054908 (2012).

[26] Z.-W. Lin and C. M. Ko, Kaon interferometry at RHIC from AMPT model, J. Phys. G **30**, S263 (2004).

[27] W. M.-Juan, C. Gang, and W. Yuan-Fang, Eccentricity and elliptic flow at fixed centrality in Au + Au collisions at $\sqrt{s_{\rm NN}} =$ 200 GeV in an AMPT model, Chin. Phys. C **37**, 014104 (2013).

[28] PHENIX Collaboration, A. Adare *et al.*, Quadrupole Anisotropy in Dihadron Azimuthal Correlations in Central $d+$Au collisions at $\sqrt{s_{NN}} = 200$ GeV, Phys. Rev. Lett. **111**, 212301 (2013).

[29] L. He, T. Edmonds, Z.-W. Lin, F. Liu, D. Molnar, and F. Wang, Anisotropic parton escape is the dominant source of azimuthal anisotropy in transport models, arXiv:1502.05572 (2015).